Electronic Supplemental Information for

A Facile Mechanochemical Route to Covalently Bonded Graphitic Carbon Nitride (g-C_3N_4) and Fullerene Hybrid toward Enhanced Visible Light Photocatalytic Hydrogen Production

*Xiang Chen, Huanlin Chen, Jian Guan, Jieming Zhen, Zijun Sun, Pingwu Du, Yalin Lu, and Shangfeng Yang**

Hefei National Laboratory for Physical Sciences at Microscale, Key Laboratory of Materials for Energy Conversion, Chinese Academy of Sciences, Department of Materials Science and Engineering, Synergetic Innovation Center of Quantum Information & Quantum Physics, University of Science and Technology of China (USTC), Hefei 230026, China

Table of Contents

S1. Raman spectra of products obtained from ball-milling a mixture of pristine g-C_3N_4 and C_{60} with and without LiOH catalyst.

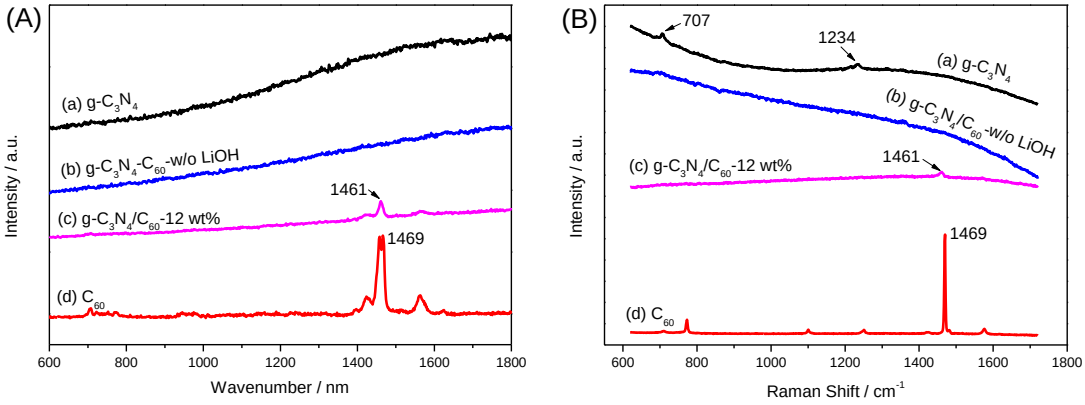

Figure S1. Raman spectra of pristine g-C_3N_4 (a), products obtained from ball-milling a mixture of pristine g-C_3N_4 and C_{60} without (b) and with (c) LiOH catalyst, and pristine C_{60} (d). The excitation laser light wavelengths are 532 nm (A) and 785 nm (B), respectively.

S2. High-resolution C1s, N1s and O1s XPS spectra.

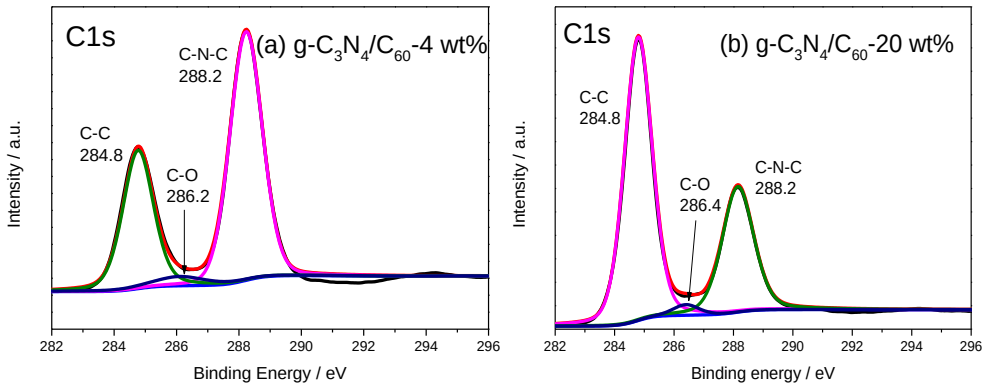

Figure S2. High-resolution C1s XPS spectra of g-C_3N_4/C_{60}-4 wt% (a) and g-C_3N_4/C_{60}-20 wt% (b).

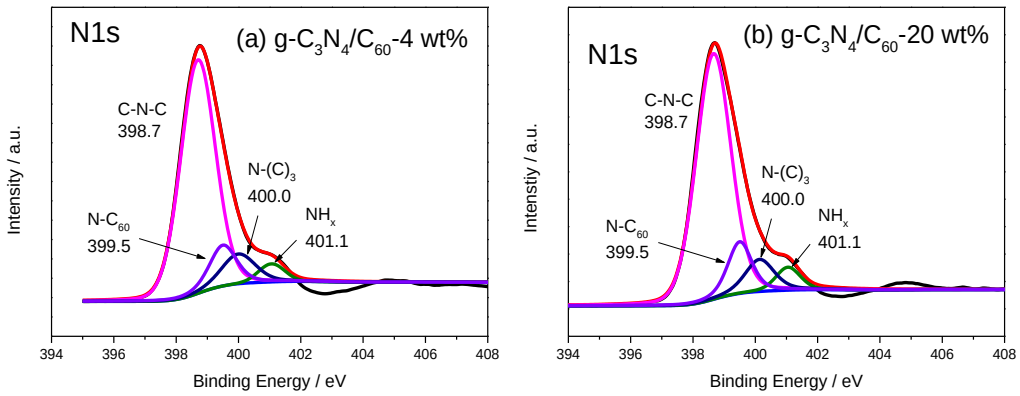

Figure S3. High-resolution N1s XPS spectra of g-C_3N_4/C_{60}-4 wt% (a) and g-C_3N_4/C_{60}-20 wt% (b).

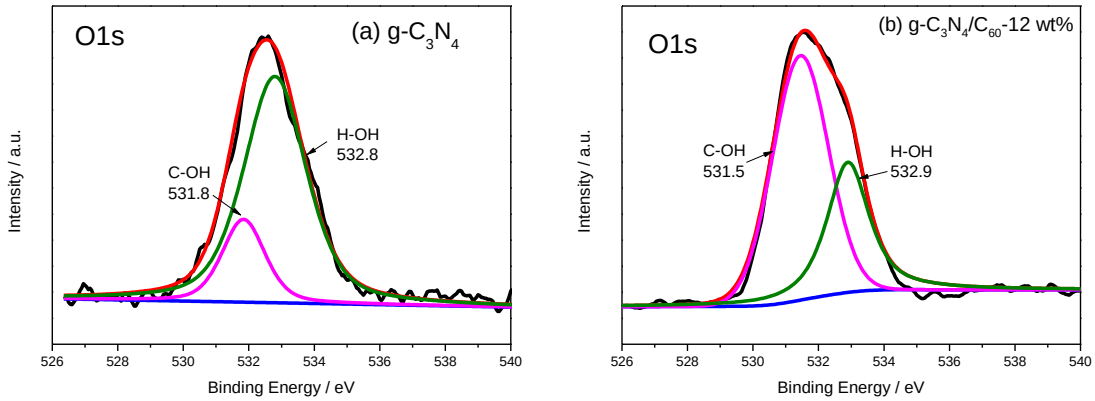

Figure S4. High-resolution O1s XPS spectra of pristine g-C_3N_4 (a) and g-C_3N_4/C_{60}-12 wt% (b).

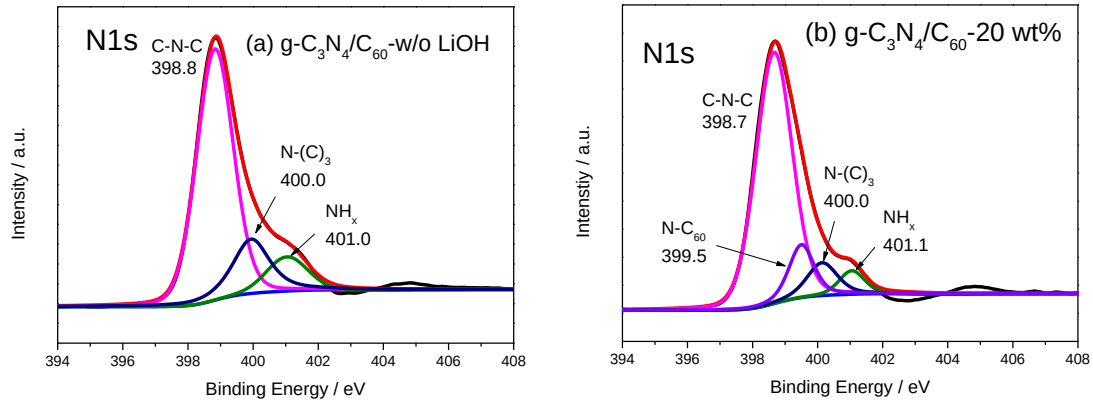

Figure S5. High-resolution N1s XPS spectra of products obtained from ball-milling a mixture of pristine g-C_3N_4 and C_{60} without (a) and with (b) LiOH catalyst.

S3. XRD patterns of products obtained from ball-milling a mixture of pristine g-C_3N_4 and C_{60} with and without LiOH catalyst.

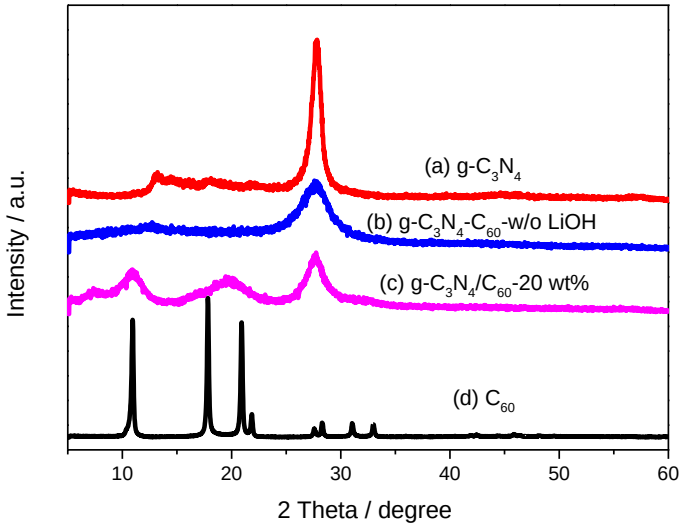

Figure S6. XRD patterns of pristine g-C_3N_4 (a), products obtained from ball-milling a mixture of pristine g-C_3N_4 and C_{60} without (b) and with (c) LiOH catalyst, and pristine C_{60} (d).

S4. TGA curves.

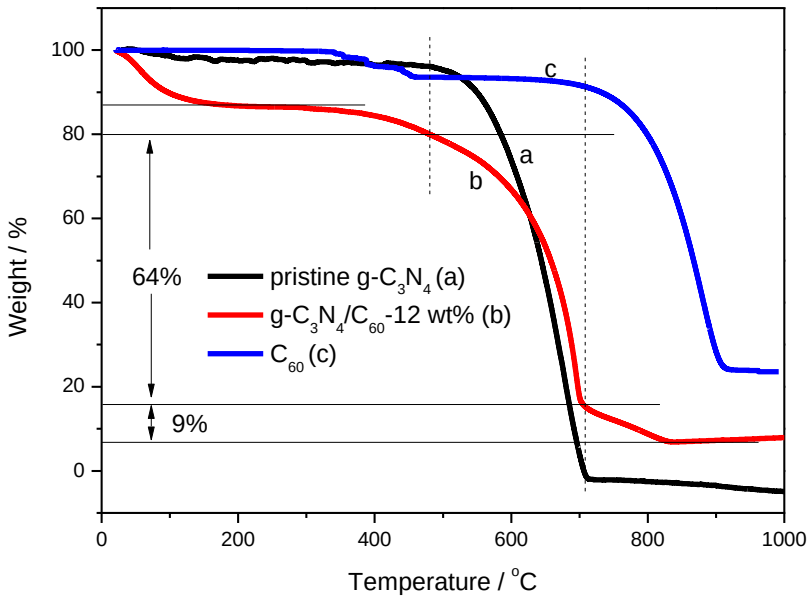

Figure S7. TGA curves of pristine g-C_3N_4 (a), g-C_3N_4/C_{60}-12 wt% hybrid (b), and C_{60} (c). The right dotted vertical line was added to aid identifying the last weight loss step (708 - 830 ^oC) corresponding to the decomposition of C_{60}.

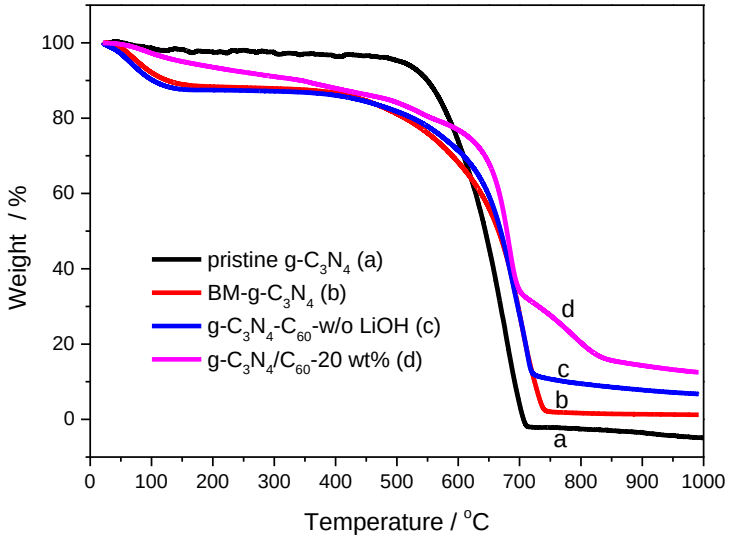

Figure S8. TGA curves of pristine g-C_3N_4 (a), pure g-C_3N_4 after ball-milling (BM-g-C_3N_4, b), products obtained from ball-milling a mixture of pristine g-C_3N_4 and C_{60} without (c) and with (d) LiOH catalyst.

S5. Schematic illustration of the formation mechanism of the g-C_3N_4/C_{60} hybrid.

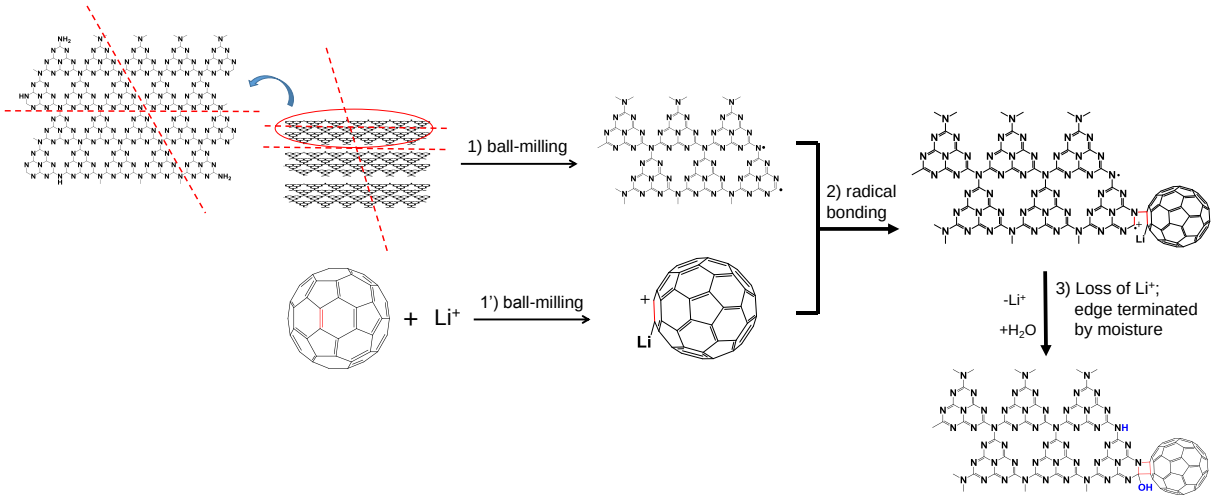

Scheme S1. A schematic illustration of the formation mechanism of the g-C_3N_4/C_{60} hybrid via the mechanochemical ball-milling in the existence of LiOH as catalyst.

S6. FTIR, Raman spectra and XRD patterns of product obtained by reaction of g-C_3N_4 with C_{60} in DMF solution.

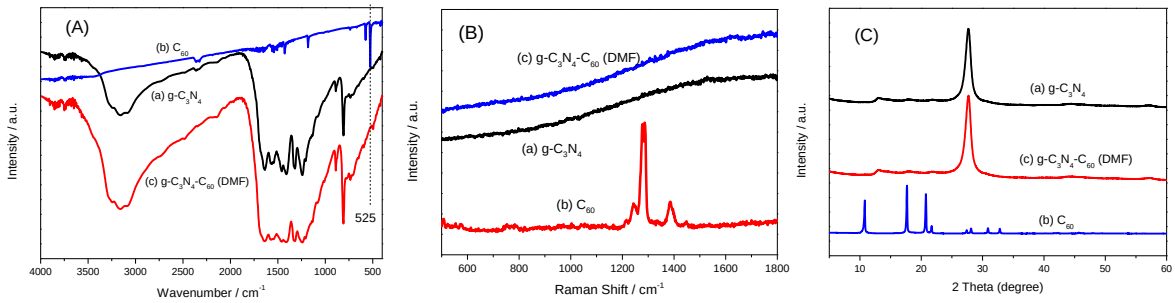

Figure S9. FTIR spectra (A), Raman spectra (B) and XRD patterns (C) of pristine g-C_3N_4 (a), C_{60} (b) and product obtained by reaction of g-C_3N_4 with C_{60} in DMF solution (g-C_3N_4-C_{60}, c).

A mixture of 200 mg pristine g-C_3N_4 and 200 mg C_{60} was dispersed in N,N-dimethylformamide (DMF) solution and stirred for 24 h under 70 ^oC, followed by Soxhlet-extraction with CS_2 for 48 h to remove the unreacted C_{60}. No C_{60} moiety was detected in the final product based on FTIR, Raman and XRD characterizations, revealing that the reaction of C_{60} with the terminal NH_x did not occur despite of the high nucleophilicity of the primary amine, and consequently covalent bonding of C_{60} with the terminal NH_x at the edge of pristine g-C_3N_4 seems unlikely.

S7. SEM image of product obtained from ball-milling pure g-C_3N_4.

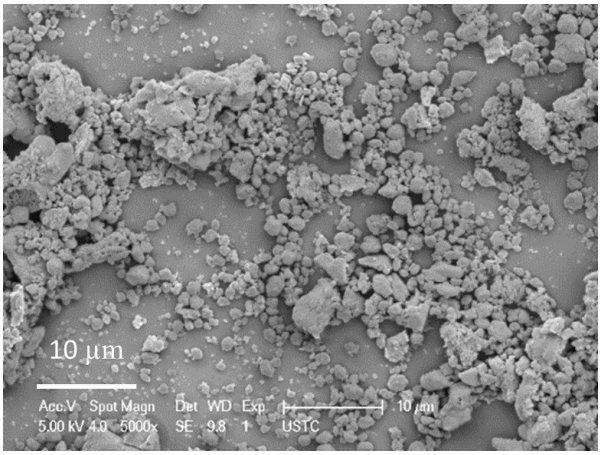

Figure S10. SEM image of product obtained from ball-milling of pure g-C_3N_4.

S8. TEM elemental mapping images of g-C_3N_4 and g-C_3N_4/C_{60} hybrid.

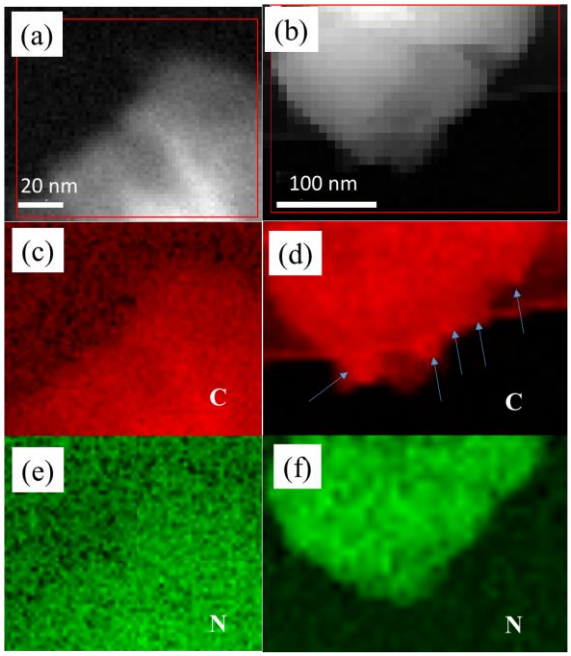

Figure S11. TEM elemental mapping images of the portion selected for pristine g-C_3N_4 (a, c, e) and g-C_3N_4/C_{60}-12 wt% hybrid (b, d, f). The corresponding C (c, d) and N (e, f) elemental mapping images are also shown.

The C elemental mapping image of g-C_3N_4/C_{60} hybrid (image d) shows the enrichment of C elements at the edges (marked by arrows), whereas such a phenomenon is not observed for N element in the N elemental mapping image of g-C_3N_4/C_{60} hybrid (image f). For the case of pristine g-C_3N_4, both C and N elements distribute uniformly without obvious enrichment at the edges (images c and e). This provides further experimental evidence on the C_{60} bonding to the cleaved edge of g-C_3N_4.

S9. Quantum efficiency and action spectra of pristine g-C_3N_4 and g-C_3N_4/C_{60} hybrid.

To measure the quantum yield for visible light H_2 evolution, 50 mg powder sample was dispersed in 100 mL aqueous solution containing 17.5 mg Eosin Y (EY) and 5 ml triethanolamine (TEOA), which was irradiated by a monochromic light using a bandpass filter (± 5 nm) for 420, 450, 475, 520, and 550 nm, respectively. The quantum efficiency (φ) is calculated according to the following equation (1):

$$\varphi = \frac{\text{number of reacted electrons}}{\text{number of incident photons}} \times 100\%$$

$$= \frac{\text{number of evolved } H_2 \text{ molecules} \times 2}{\text{number of incident photons}} \times 100\% \quad (1)$$

Where the number of incident photons (N_{ph}) can be calculated from the power of the incident light (P_{ph}, 0.194, 0.205, 0.202, 0.305 and 0.225 J/s for 420, 450, 475, 520, and 550 nm, respectively), which was calibrated by an irradiatometer (FZ-A, Beijing Normal University Optical Instrument), according to equation (2) (see Figure S12):

$$N_{ph} = P_{ph} \times t / (hc/\lambda) = P_{ph} \times t \times \lambda / (hc) \quad (2)$$

Where t is the irradiation time, λ is the wavelength of the incident light, h is planck constant, c is the speed of light in vacuum.

Table S1. Quantum efficiencies (Φ) of different samples with (w) or without (w/o) Pt cocatalyst and EY photosensitizer measured under irradiation with visible light at λ = 420 nm.

sample	condition		quantum efficiency
	Pt (0.3 wt%)	EY (35 wt%)	(Φ)
pristine g-C_3N_4	w/o	w	0.072%
g-C_3N_4/C_{60}-12 wt%	w/o	w	0.20%
no (control)	w	w	6.95%
pristine g-C_3N_4	w	w	6.79%
g-C_3N_4/C_{60}-12 wt%	w	w	6.97%
pristine g-C_3N_4	w	w/o	0.037%
g-C_3N_4/C_{60}-12 wt%	w	w/o	0.051%

Without the existence of Pt cocatalyst, Φ of g-C_3N_4/C_{60}-12 wt% hybrid is 0.20% (with the existence of EY photosensitizer), which is about 2.8 times of that for pristine g-C_3N_4 (0.072%). Such an enhancement ratio is consistent with that measured for H_2 production rate (about 4.0 times), confirming that covalently bonding of C_{60} onto g-C_3N_4 can indeed result in enhanced visible light photocatalytic H_2 production.

We also measured and compared the quantum efficiencies (Φ) of g-C_3N_4/C_{60}-12 wt% hybrid and pristine g-C_3N_4 under different conditions with the existence of Pt cocatalyst (measured under irradiation with visible light at λ = 420 nm). Surprisingly, with the co-existence of both Pt cocatalyst and EY photosensitizer, the measured Φ of g-C_3N_4/C_{60}-12 wt% hybrid and pristine g-C_3N_4 (6.97% and 6.79%, respectively) are quite comparable to that obtained for the control sample (only Pt cocatalyst + EY photosensitizer, 6.95%). This suggests that in this case the visible light H_2 production is primarily contributed by EY. Furthermore, without the existence of EY photosensitizer, the measured Φ of g-C_3N_4/C_{60}-12 wt% hybrid and pristine g-C_3N_4 (0.051% and 0.037%, respectively) with the existence of Pt cocatalyst only dramatically decrease, and are even lower than that measured without Pt cocatalyst (0.072%). This confirms further the importance of EY photosensitizer which plays the role of sensitizer for extending the spectral response region as discussed already in the main text.

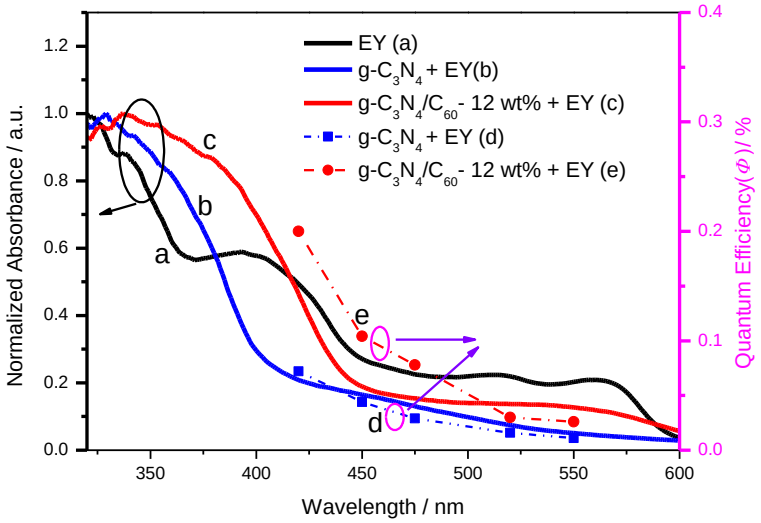

Figure S12. UV-VIS diffuse reflectance spectra of EY (a), g-C_3N_4+EY (b) and g-C_3N_4/C_{60}-12 wt%+EY (c), and action spectra for H_2 evolution of g-C_3N_4+EY (d) and g-C_3N_4/C_{60}-12 wt%+EY (e) from an aqueous triethanolamine (TEOA) solution under visible light irradiation of 300 W Xe-lamp using a bandpass filter for 420, 450, 475, 520, and 550 nm, respectively.

S10. Typical time courses of H_2 production based on pristine g-C_3N_4 and g-C_3N_4/C_{60}-12 wt% hybrid.

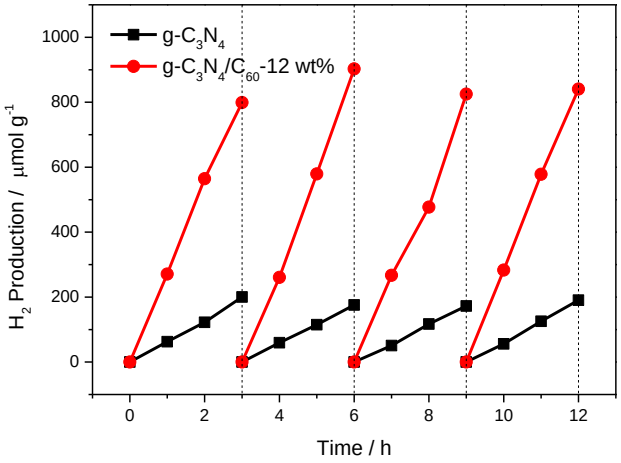

Figure S13. Typical time courses of H_2 production based on pristine g-C_3N_4 and g-C_3N_4/C_{60}-12 wt% hybrid. The measurements were carried out in an aqueous solution (containing TEOA as a hole scavenger and EY as the photosensitizer) evacuated per 3 h without renewing the hole scavenger under visible light (λ > 420 nm) irradiation of 300 W Xe-lamp.

S11. Visible light photocatalytic H_2 production rates of different control samples.

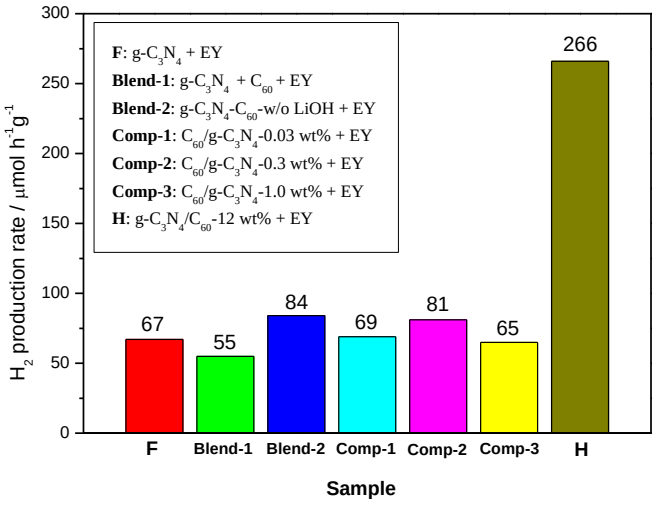

Figure S14. Photocatalytic H_2 production rates of different samples measured in 5 vol% TEOA aqueous solution in the presence of EY for 3 h under visible light (λ > 420 nm) irradiation of 300 W Xe-lamp. **Blend-1**: a physical blend of g-C_3N_4:C_{60} (64:9, w/w); **Blend-2**: a mixture of pristine g-C_3N_4 and C_{60} powders ball-milled without LiOH catalyst (g-C_3N_4-C_{60}-w/o LiOH). **Comp-1, 2, 3**: C_{60}/g-C_3N_4 composites with different C_{60}/dicyandiamide mass ratios (0.03 wt%, 0.3 wt% and 1.0 wt% for **Comp-1, 2, 3**, respectively) using the method reported in ref. [27].

S12. Diffuse reflectance UV-vis absorption spectra of pristine g-C_3N_4 and g-C_3N_4/C_{60}-12 wt% hybrid.

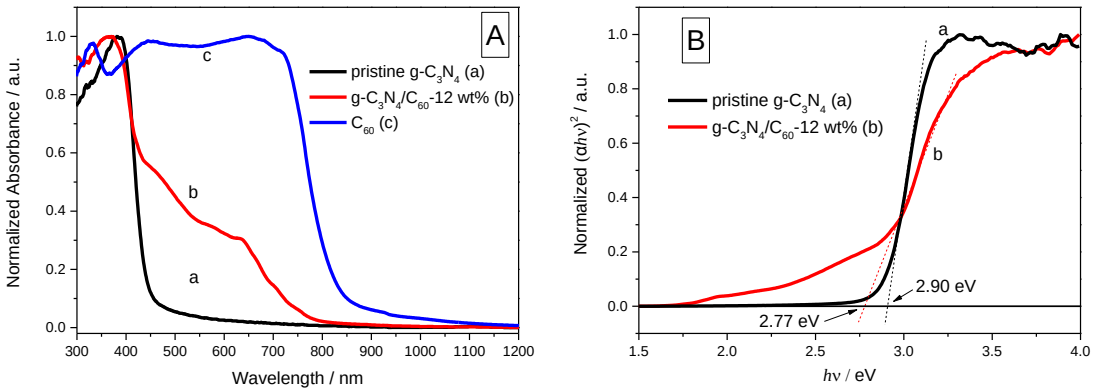

Figure S15. Diffuse reflectance UV-vis absorption spectra (A) and $(\alpha h\nu)^2$ versus $h\nu$ curves (B) of pristine g-C_3N_4 (a) and g-C_3N_4/C_{60}-12 wt% hybrid (b), and C_{60} (c).

S13. BET surface areas of pristine g-C_3N_4 and g-C_3N_4/C_{60} hybrid calculated from the nitrogen adsorption-desorption isotherms.

Table S2. BET surface areas of pristine g-C_3N_4, BM-g-C_3N_4, g-C_3N_4/C_{60}-12 wt% and g-C_3N_4/C_{60} w/o LiOH.

sample	BET Surface area (m^2/g)
pristine g-C_3N_4	12.5
BM-g-C_3N_4	16.1
g-C_3N_4/C_{60}-12 wt%	16.6
g-C_3N_4-C_{60}-w/o LiOH	16.9

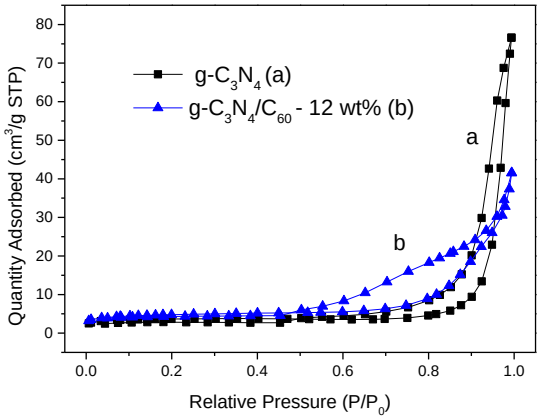

Figure S16. Nitrogen adsorption–desorption isotherms of g-C_3N_4 (a) and g-C_3N_4/C_{60} hybrid (b).

S14. Electrical Conductivities of pristine g-C_3N_4 and g-C_3N_4/C_{60} hybrid.

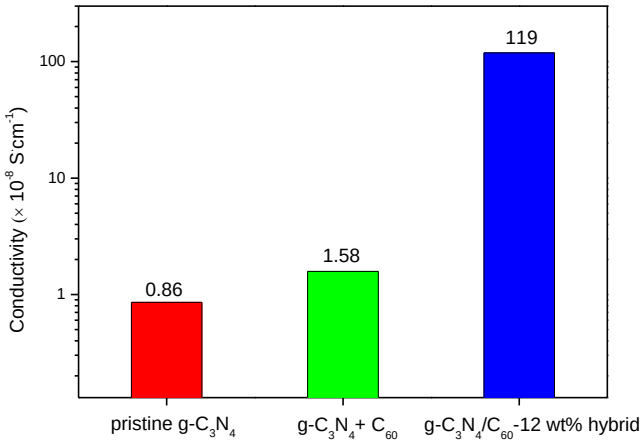

Figure S17. Electrical conductivities of the pristine g-C_3N_4, g-C_3N_4/C_{60}-12 wt% and a physical blend of g-C_3N_4:C_{60} (g-C_3N_4 + C_{60}). Samples were pressed into tablets with the same thickness of approximately 1 mm.

S15. Mott–Schottky plots of pristine g-C_3N_4 and g-C_3N_4/C_{60} hybrid.

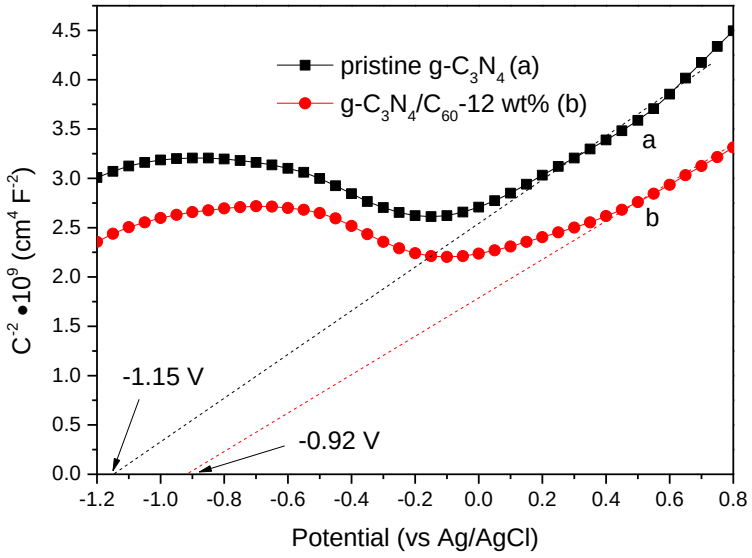

Figure S18. Mott-Schottky (MS) plots of pristine g-C_3N_4 (a) and g-C_3N_4/C_{60}-12 wt% hybrid (b) film electrodes. The MS plots were obtained in a 0.1 M Na_2SO_4 aqueous solution at a frequency of 1 kHz. The flat band potentials of g-C_3N_4 (a) and g-C_3N_4/C_{60}-12 wt% hybrid (b) are determined to be -1.15 and -0.92 V *vs.* Ag/AgCl, which correspond to -0.95 and -0.72 V *vs.* NHE, respectively, according to an equation E(NHE) = E(Ag/AgCl) + 0.198.

S16. PL spectra of pristine g-C_3N_4 and g-C_3N_4/C_{60} hybrid.

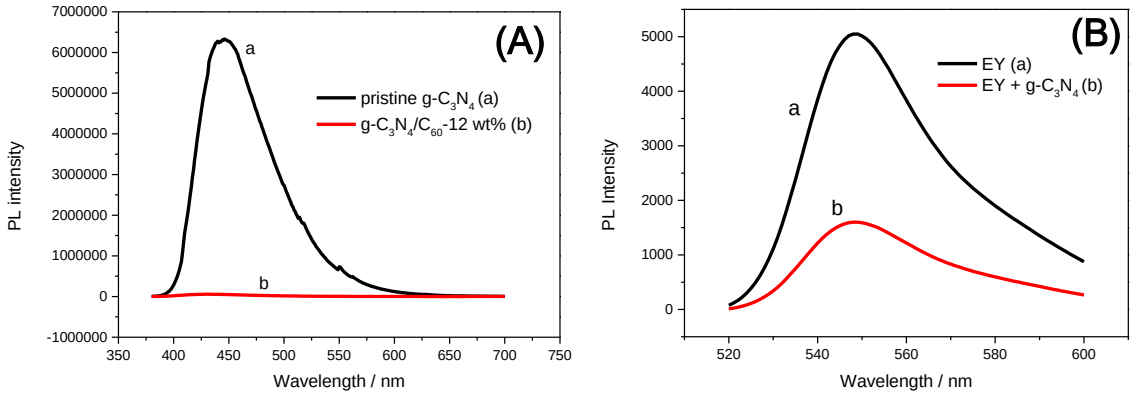

Figure S19. (A) PL spectra of pristine g-C_3N_4 (a) and g-C_3N_4/C_{60}-12 wt% hybrid (b) under the excitation wavelength of 360 nm. **(B)** PL spectra of EY (a) and EY + g-C_3N_4 (b) under the excitation wavelength of 520 nm.